Supplementary Information

Disordered Mosaic Metasurfaces with Scalable Functional Density

Chi Li,[1,#] Changxu Liu,[2,#,*] Cade Peters[3], Haoyi Yu[1], Stefan A. Maier,[1,4] Andrew Forbes,[3] Haoran Ren[1,*]

[1] School of Physics and Astronomy, Monash University, Melbourne, VIC 3800, Australia

[2] Centre for Metamaterial Research & Innovation, Department of Engineering, University of Exeter, Exeter EX44QF, United Kingdom

[3] School of Physics, University of Witwatersrand, Johannesburg, South Africa

[4] Department of Physics, Imperial College London, London SW7 2AZ, United Kingdom

[#] These authors contribute equally

[*] To whom correspondence E-mails:

C.C.Liu@exeter.ac.uk;

Haoran.ren@monash.edu.

CONTENTS

Supplementary Note 1. MATHEMATICAL EXPOSITION

A. Calculation of Strehl Ratio

To quantify the focusing performance of a metalens, we use the Strehl Ratio (SR), a widely accepted figure of merit that compares the actual point spread function (PSF) of a system with that of an ideal diffraction-limited reference.

In our case, we consider the PSF on the focal plane (x, y). Both the actual and ideal PSFs are first normalized such that their total integrated intensity equals 1, $\iint PSF(x,y)dx\,dy = 1$. Then let A and B be the maximum value of the actual and ideal PSFs. The Strehl Ratio is then given by Ref. [**1**]:

$$SR = \frac{A}{B}$$

This definition provides a direct measure of how much the peak focusing intensity deviates from the ideal case. When the focusing is ideal (i.e., diffraction-limited), the PSF remains tightly confined and the SR approaches 1. However, as the PSF spreads, the peak intensity decreases while the total energy remains constant. Consequently, the SR deviates from unity and provides a sensitive indicator of the degradation in focusing performance.

B. Quantification of Spatial Disorder

To quantitatively characterize the degree of spatial disorder in metasurface sampling patterns, we employ **Moran's spatial autocorrelation index** (*I*), a statistical measure commonly used to assess spatial clustering.

We represent the metasurface as a two-dimensional $N \times N$ binary matrix $X = \{x_i\}$, where each element $x_i \in \{0,1\}$ denotes the state of a meta-pixel (inactive = 0, active = 1). The matrix is initialized with an equal number of 0s and 1s, taking right half and left half of the matrix, corresponding to an area usage fraction of $p = 0.5$. In the initial ordered state, all 1s and 0s are spatially clustered. To introduce disorder, we randomly swap pairs of 1s and 0s. As the number of swaps increases, the spatial distribution of active pixels becomes progressively more randomized. Maximum disorder is reached when approximately half of the 1s are redistributed.

Moran's *I* is computed as follows Ref. [**2**]:

$$I = \frac{N^2}{W} \cdot \frac{\sum_i \sum_j w_{ij}(x_i - \bar{x})\left(x_j - \bar{x}\right)}{\sum_i (x_i - \bar{x})^2}$$

where $\bar{x}$ is the mean, w_{ij} is the spatial weight between elements i and j (defined as 1 for adjacent and 0 otherwise) and $W = \sum_i \sum_j w_{ij}$.

The index ranges from $I = 1$ for perfectly clustered (ordered) configurations to for $I = 0$ completely random (disordered) patterns. This formulation allows us to quantitatively monitor the transition from order to disorder and correlate spatial arrangement with optical performance metrics SR.

Block Entropy is an alternative measurement of the disorder. Entropy, in the context of information theory, quantifies the amount of uncertainty or disorder in a system. In the context of a 2D binary matrix, the global Shannon entropy will remain constant if the total number of 1s (representing used pixels) and 0s (representing unused pixels) is preserved—regardless of how they are arranged spatially. Therefore, global entropy fails to capture spatial order or structure. To overcome this, we introduce block entropy, a localized variant of Shannon entropy that probes spatial randomness within small regions of the matrix. The matrix is partitioned into non-overlapping square blocks of size *M*. Within each block, we compute the local Shannon entropy as above, using the relative frequency p_i of 1s in that block. The overall block entropy $\overline{H}_b$ is then defined as the average entropy across each H_b:

$$H_b = \frac{1}{M^2} \sum_{i=1}^{M^2} [-p_i \log_2 p_i - (1 - p_i) \log_2 (1 - p_i)]$$

Supplementary Fig. 1 shows the relationship between Moran's *I* and block entropy during order to disorder transition. As the decrement of the values of the Moran's *I*, the block entropy also increases. However, block entropy does not alone distinguish between random and structured mixtures.

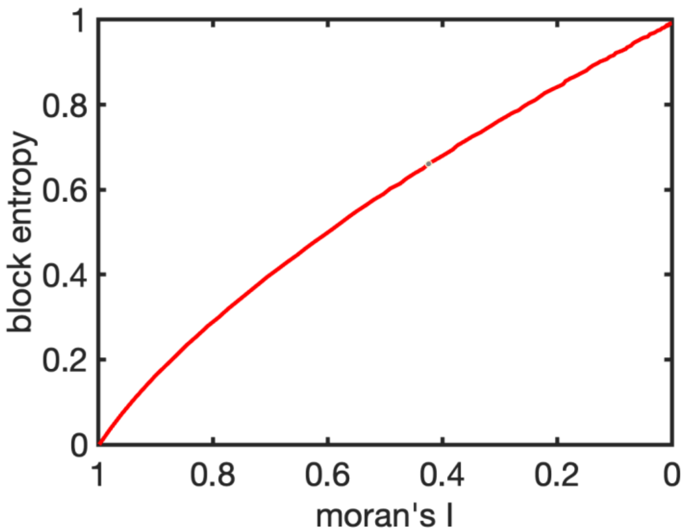

Supplementary Fig. 1. Order to disorder transition. Block entropy *vs* Moran's *I* during order to disorder transition.

Supplementary Note 2. ENERGY EFFICIENCY AND ACHROMATIC FOCUSING OF DMM-BASED ACHROMATIC LENS

A. Concentric ring configuration and grid sampling

Analogous to the sector-type configuration, the concentric ring arrangement exhibits a similar reduction in SR as the area usage decreases. As schematically illustrated in the inset of Supplementary Fig. 2, for an aperture of radius R, the utilized region (highlighted in red) gradually shrinks toward R/2 as the effective area usage is reduced.

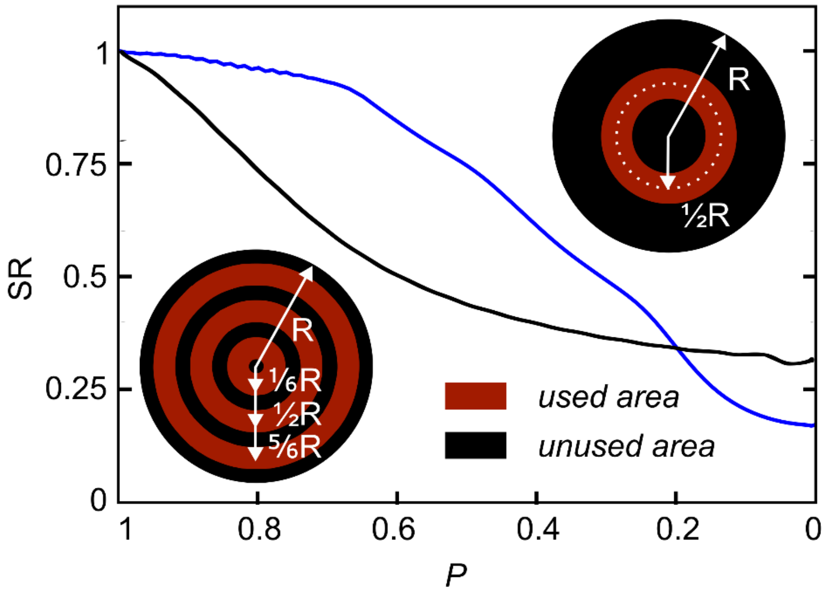

Supplementary Fig. 2. Sampling for the concentric ring configuration. Strehl ratio of a metalens as a function of *p* for one (upper, blue curve) and multiple (lower, black curve) concentric ring configurations.

To select a fraction of an area, one can employ a regular grid sampling method. However, this approach introduces inherent spatial periodicity, which may disrupt a phase map that is not uniformly distributed, such as in a lens. We conducted numerical simulations with a fixed area usage of p = 0.0625. As illustrated in Supplementary Figs 3, 1/16 of the pixels in a grayscale phase map of a lens were sampled using different methods. Despite using only 1/16 of the pixels, both sampling techniques successfully focused light onto the designed focal plane with comparable intensity at their focal spots. However, the uniform grid sampling lens exhibited numerous diffraction patterns, which were also focused onto the focal plane. In contrast, the randomly sampled lens demonstrated excellent light focusing, matching the performance of an ideal lens with full-area usage, with light homogeneously concentrated at a single focal spot.

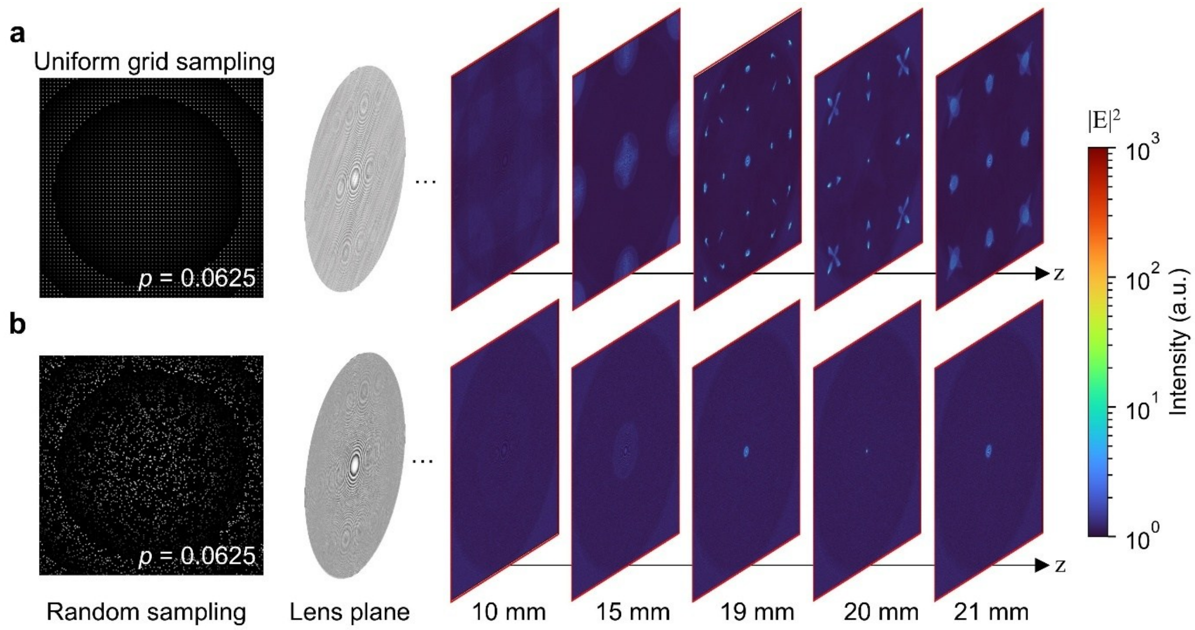

Supplementary Fig. 3. Optical lens with an area usage of *p* = 0.0625, sampled using different methods. (**a**) Uniform grid sampling. (**b**) Random sampling. The displayed pixels are zoomed in from the complete lens phase map to clearly illustrate the distinct sampling methods. All colour plots are normalized to the maximum intensity at the focal spot of (b) with a focal length of f = 20 mm.

B. Energy efficiency of the disordered sampling

While the use of disorder allows the metalens to maintain focusing quality, as quantified by the *SR,* even at low area usage fractions (*p*), the overall energy efficiency decreases with reducing *p*. To evaluate this, we compute the optical power contained within a circular region centred at the focal spot, with a diameter equal to three times the full width at half maximum (FWHM) of the ideal PSF. The results are summarized in Supplementary Fig. 4a, showing a near-linear decline in collected power as *p* decreases. Supplementary Fig. 4b presents the power measured within the 3×FWHM region for DMM-based metalenses with varying functional density D_f. Although the absolute power decreases with increasing D_f, the spectral uniformity of the focusing, i.e., the power variation across wavelengths, shows a significant improvement. This highlights a key trade-off: while disordered sampling reduces local energy concentration, it enables more uniform performance across a broader spectral range.

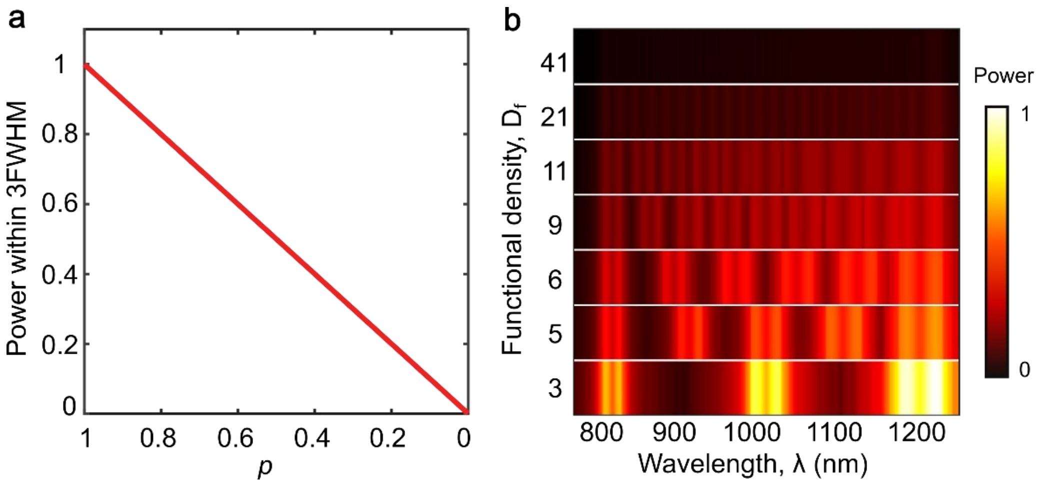

Supplementary Fig. 4. **Energy efficiency of disordered sampling and DMM-based metalenses**. (**a**) Collected optical power within a circular region (diameter = 3×FWHM of the ideal PSF) as a function of area usage fraction *p*. (**b**) Power within the 3×FWHM region for DMM-based metalenses with different functional densities. Although absolute power decreases with higher D_f., the spectral uniformity of power distribution improves significantly, indicating more consistent performance across the target wavelength range.

C. DMM-based achromatic lens using large D_f

As illustrated in Supplementary Fig. 5a (upper panel), each phase pixel is modelled with unity transmission for its designated spectral band and zero transmission outside it. This assumption enables crosstalk-free synthesis of achromatic focusing across a target spectral range, governed by the D_f and the bandwidth of each constituent function (Supplementary Fig. 5a, lower panel). Supplementary Fig. 5b quantitatively illustrates the enhancement of achromatic performance with increasing functional density D_f. Both the average Strehl ratio across the spectral range (800-1200 nm) and its spectral uniformity improve as D_f increases, that is, the mean SR increases while the standard deviation decreases. Remarkably, even at a high functional density of $D_f = 41$, where each function occupies only a small portion of the total area, the quality of the PSF remains well preserved. Supplementary Fig. 5c confirms this by displaying PSFs at five representative wavelengths, all exhibiting high-fidelity focusing performance.

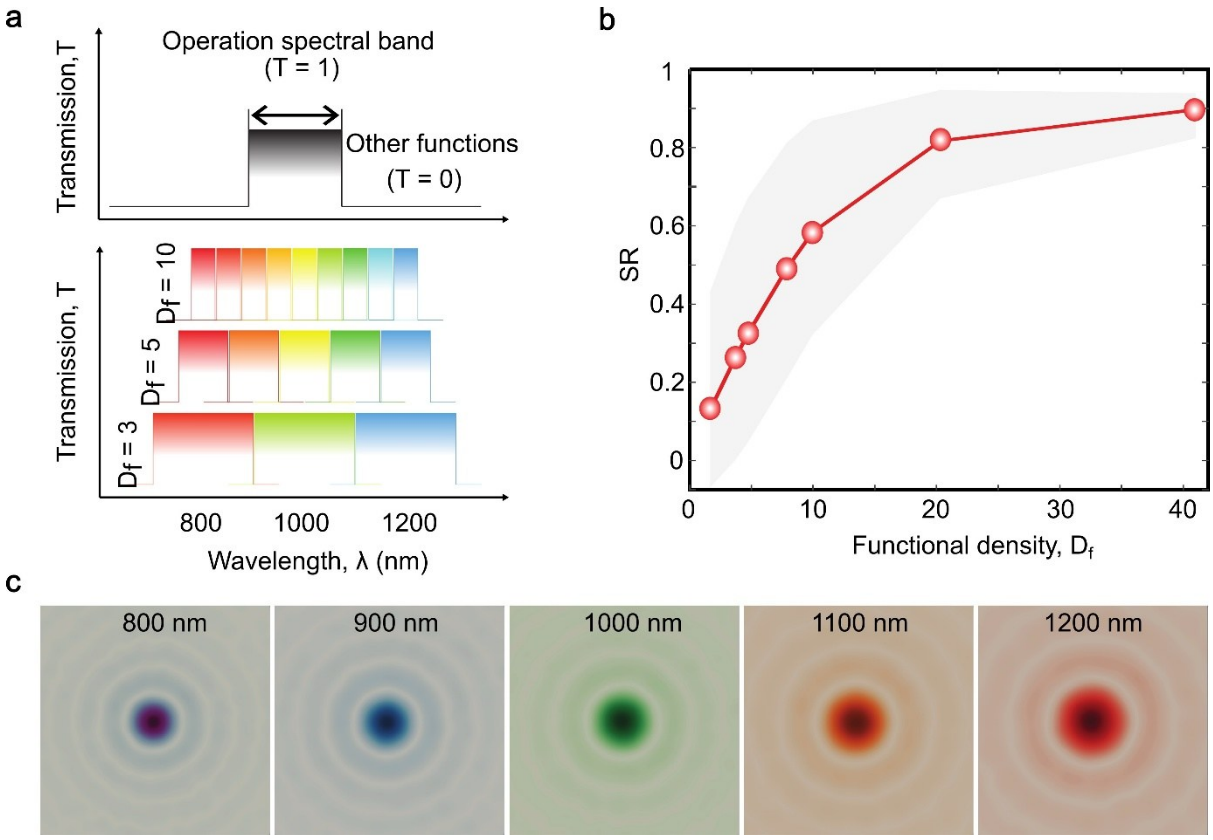

Supplementary Fig. 5. Achromatic performance of the DMM-based metalens as a function of functional density. (**a**) Schematics of an ideal bandpass filter for a single function (top), and a DMM-based achromatic metalens comprising multiple crosstalk-free bandpass filters (bottom). (**b**) Average Strehl ratio (red solid circle) and corresponding standard deviation (shaded area) across the wavelength range of 800-1200 nm, plotted against the functional density (D_f). (**c**) Normalized PSFs at five representative wavelengths for a metalens with $D_f = 41$ as the transverse plane.

D. Multiwavelength light focusing across the VIS, NIR and MIR spectral domains

Supplementary Fig. 6 presents simulated PSFs of a multiwavelength metalens operating at 473 nm, 514 nm, 633 nm, 1.35 µm, 1.55 µm, 2.05 µm, 2.94 µm, 3.4 µm, and 4 µm, sharing the same focal distance. Each metalens function occupies 1/9 of the aperture area. These wavelengths were selected because of their relevance to diverse applications, including astronomical instrumentation, fluorescence imaging, biomedical diagnostics, hydrocarbon sensing, and thermal/atmospheric monitoring (see Supplementary Table 1). The PSFs are magnified for clarity.

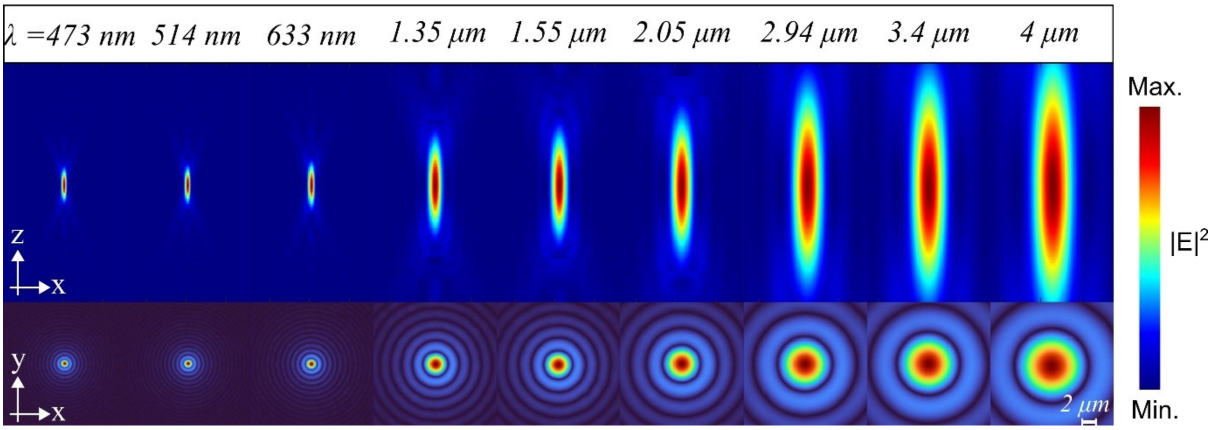

Supplementary Fig. 6. Multiwavelength light focusing across the VIS, NIR and MIR spectral domains. The top and bottom panels show the PSFs in the longitudinal and transverse planes, respectively.

Supplementary Note 3. IMPLEMENTATION OF DMM-BASED ACHROMATIC METALENS AND MULTIFUNCTIONAL DISPLAY

A. Numerical simulation of nonlocal resonance in meta-pixels

We numerically calculated the non-local resonance in a metasurface with reduced dimensions, using square unit cells comprising two "T"-shaped rectangles. The modelling was implemented in COMSOL with periodic ports and boundary conditions. A padding distance exceeding one wavelength was added to isolate each meta-pixel from adjacent periods. As the meta-pixel size increased, specifically the number of square cells (n × n), additional diffraction orders were included to maintain high calculation precision. As shown in Supplementary Fig. 7, the cross-circular polarisation filtered transmission spectra exhibit a distinct peak starting at n = 5, which gradually shifts to longer wavelengths with increasing transmission intensity, approaching the ideal non-local metasurface scenario with an infinite number of cells (no additional padding). In the 9×9 meta-pixel configuration, a strongly confined electric field distribution was observed at the centre of the metasurface, displaying the same field pattern characteristic of the non-local scenario (plotted for 9×9 square cells).

We note that further reduce the padding gaps to below one wavelength may introduce inter-pixel coupling, which can slightly modify the resonance intensity and spectral position (Supplementary Figs. 7c-e). However, since the proposed function-isolation strategy operates within a designed bandwidth, such small perturbations are not expected to affect the intended functionality.

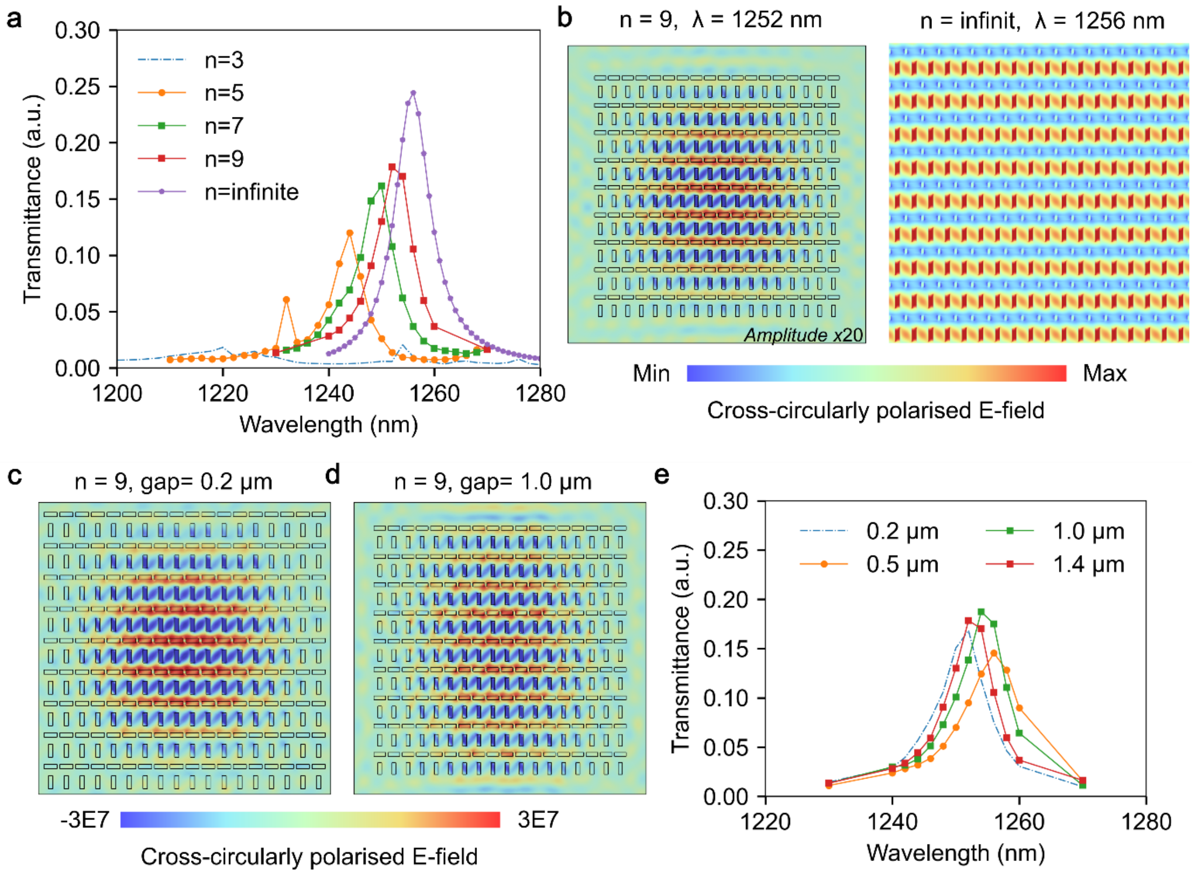

Supplementary Fig. 7. Numerical simulation of nonlocal resonance in meta-pixels. (**a**) Cross-circular polarisation spectra for meta-pixels with unit square cell number of 3x3, 5x5, 7x7, 9x9. Perfect nonlocal response with infinite number case plotted for reference. (**b**) Cross-circularly polarised electric-field distribution for a 9x9 meta-pixel (with a spacing gap of 1.4 μm) and ideal nonlocal metasurface respectively. The electric-field amplitude multiplied 20 in the n = 9 plot. (**c, d**) Cross-circularly polarised E-field distribution in a 9x9 meta-pixel for subwavelength gap sizes of 200 nm (**c**) and 1 um (**d**). (**e**) Resonance characteristics as a function of gap size.

B. Optical setup for the PSF characterisation

For metalens PSF characterization, we utilized a custom-built lens characterization setup, as schematically depicted in Supplementary Fig. 8. The sample was mounted on a translation stage with a maximum travel distance of 300 mm (DDS300, Thorlabs, not shown in figure). A linear polarizer and a quarter-wave plate were positioned to convert incident light into circular polarisation. Transmitted light was collected using a 10x objective lens (Nikon, NA = 0.3). Before the tube lens, a cross-circular polarizer, consisting of a quarter-wave plate and a linear polarizer, was placed to block the primary incident light. The camera and linear translation stage were synchronized using a customwritten program, enabling the camera to capture one image per 1-μm step of the stage movement. During the measurement, the step size was set to 1 μm.

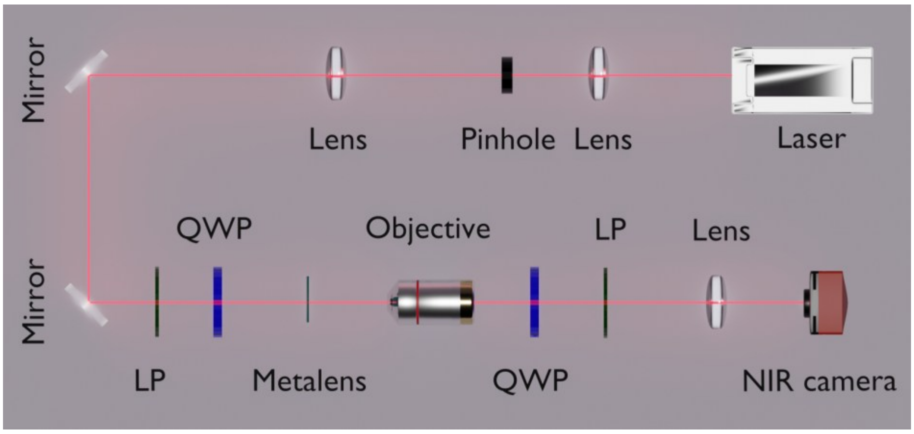

Supplementary Fig. 8. Optical setup for PSF characterisation. Schematic of metalens PSF measurement setup.

C. Q factor analysis of resonant meta-pixels

All individual meta-pixels, with spectra shown in Figure 3d, were analysed by fitting with a Gaussian function. As presented in Supplementary Fig. 9, the average Q-factor is approximately 150, with values increasing as the number of unit cells increases. The Q-factor remains relatively stable across the measured scaling factor range of 0.7 to 1.0.

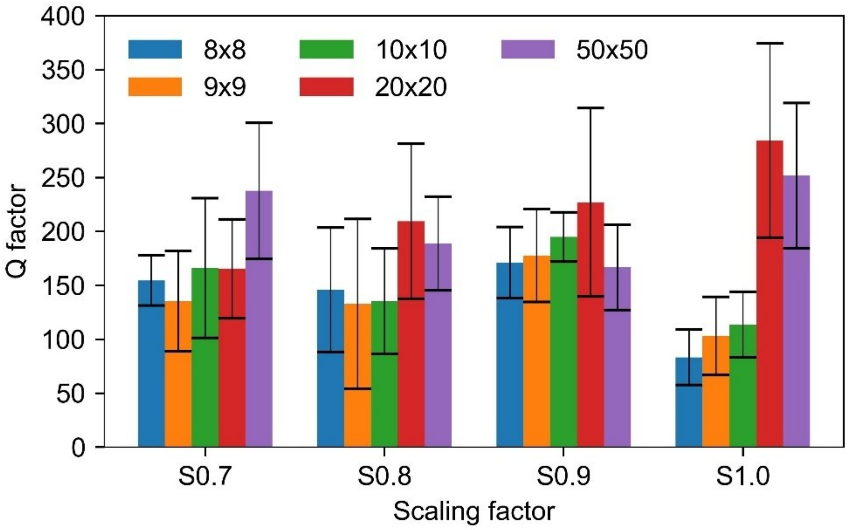

Supplementary Fig. 9. Meta-pixel Q factor statistics. The error bars represent one standard deviation across 12 datasets.

D. Experimental PSF profiles in Figure 4

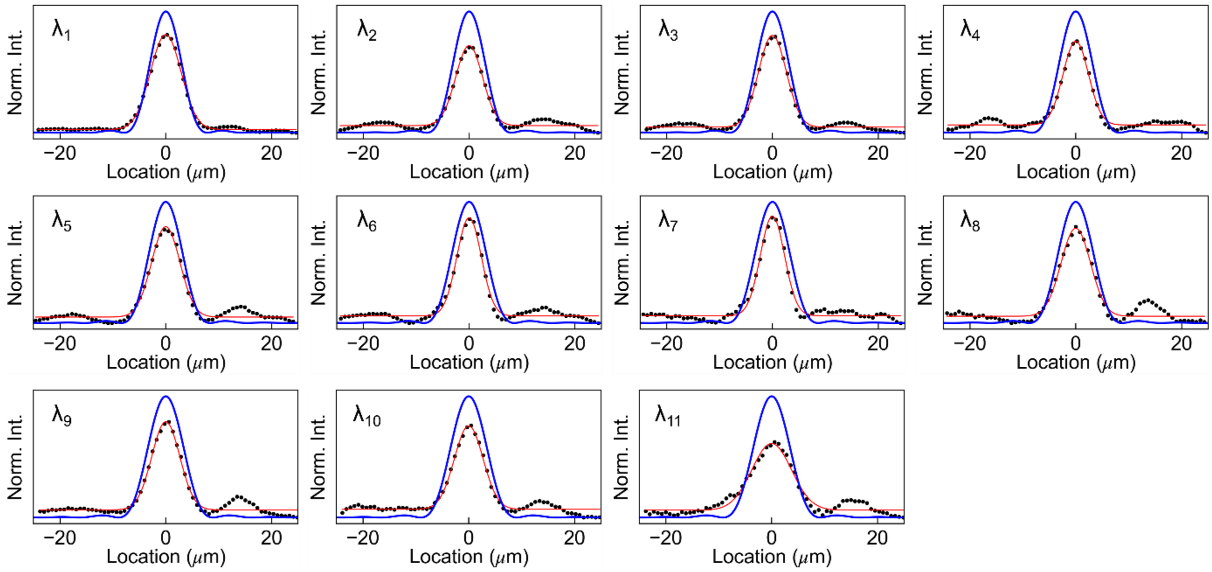

Supplementary Fig. 10. **Experimental and theoretical PSF profiles.** Black dots represent experimental data, red curves denote Gaussian fits to the main lobe, and blue curves correspond to theoretical predictions.

E. Nonlocal-type phase meta-pixel

Nonlocal-type meta-pixels, with their individual built-in structures, can provide the required phase distribution in space while maintaining resonance (Ref. [3]). Instead of applying a fixed rotation angle across the entire meta-pixel area, these meta-pixels can function as multiple phase pixels. Below, we present simulations of a varying-phase meta-pixel for the lens function used in Figure 4. To achieve this, we randomly selected 1/11 of the lens area (1000 x 1000 pixels) as a spatial mask and assigned each masked pixel with corresponding varying phases within the 8.1 μm area of the phase map (Supplementary Fig. 11). Due to the significantly increased number of phase pixels in this configuration, light focuses more efficiently at the focal spot, resulting in approximately fourfold peak intensity enhancement.

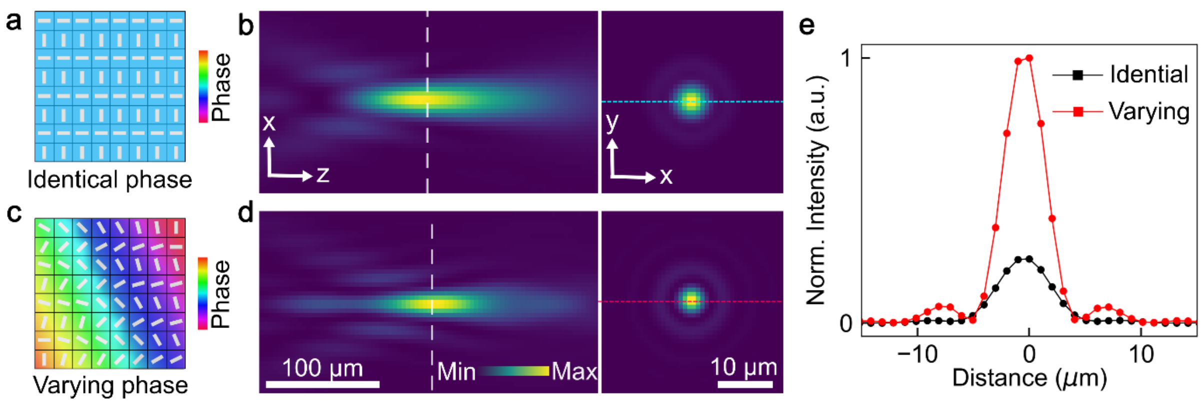

Supplementary Fig. 11. Nonlocal-type phase meta-pixel. (**a**) Schematic of applying identical phases across an entire meta-pixel. (**b**) Electric field power distribution in the x-z plane and x-y planes around the focal spot. (**c**) Schematic of applying varying phases across an entire meta-pixel. (**d**) Electric field power distribution in the x-z plane and x-y planes around the focal spot. (**e**) PSF curves for identical phase and varying phase configurations.

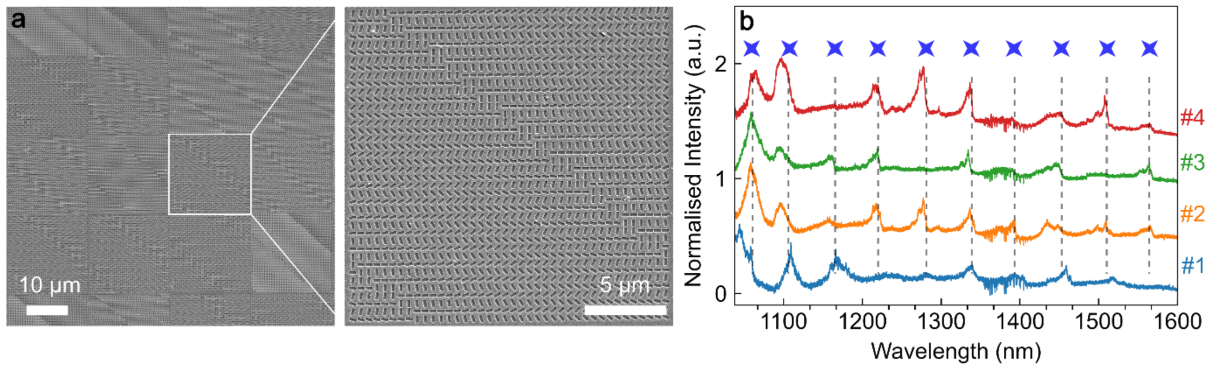

Supplementary Fig. 12. Ten-share DMM-based metalens with spatially varying phase profiles. (**a**) SEM images of the metalens showing meta-atoms with different rotation angles in a meta-pixel. (**b**) Transmission spectra measured at four different spatial locations on the metalens. Stars and dashed lines indicate the observed resonances. The spectra are normalised and vertically offset for clarity.

Geometric-phase qBICs are employed in the DMM metalens to achieve high-Q wavefront control, with the phase modulation precisely defined by the rotation angle of individual meta-atoms. To verify the operation of spatially varying phase meta-pixels, transmission spectra were measured at four different locations across a 10-share DMM-based metalens with spatially varying phase configurations (Supplementary Fig. 12). Each measured spectrum exhibits multiple resonances, ranging from a few to up to ten distinct peaks. Due to the random spatial distribution of functional meta-pixels, the number of observable resonances varies between locations, as expected. The observation of all ten resonances across different positions confirms the efficient operation of spatially varying phase meta-pixels in the DMM-based metalens.

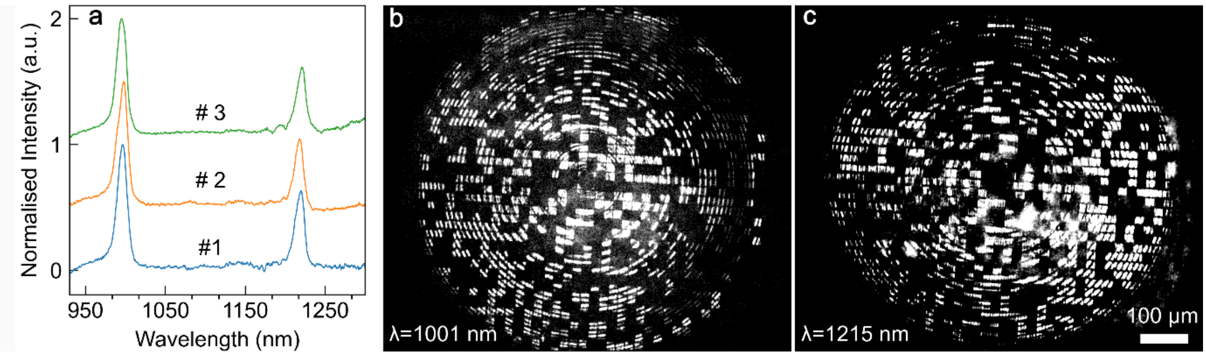

Supplementary Fig. 13. **Resonance and imaging of the two-share DMM-based metalens**. (**a**) White-light transmission spectrum. (**b**) Imaging of the metalens surface under 1006 nm laser illumination. (**c**) Imaging of the metalens surface under 1215 nm laser illumination.

We measured the focusing efficiency of a dual-wavelength DMM-based metalens using a two-share sample with a diameter of 800 μm. The two shares were designed to operate at wavelengths of 1000 nm and 1200 nm, respectively. Two sharp resonances were observed at central wavelengths of 1001 nm and 1215 nm (Supplementary Fig. 13a), with slightly shifted resonances compared to our design due to fabrication imperfections. The focusing efficiency is 25.4% and 37.5% respectively, leading to an average efficiency of about 32% for each share. This efficiency number is comparable to previous small-scale achromatic metalenses [Refs. 4-6].

Supplementary Fig. 13b and 13c show the images of the metalens surface at two resonant wavelengths. They reveal complementary activation patterns of the meta-pixels, indicating effective function isolation in the DMM-based metalens. We note that some meta-pixels near the lens edges may not be fully activated due to slight resonance detuning, as the laser used for illumination has a narrow bandwidth of approximately 2.5 nm. The above focusing efficiency is calculated under these two illumination conditions.

F. Simulated single-lens imaging

To evaluate the imaging performance, we conduct single-lens imaging simulation (Supplementary Fig. 14a). A three-share DMM-based metalens operating at 1000 nm, 1200 nm, and 1400 nm was considered, with a reduced diameter of 3 mm and a focal length of 10 mm to limit computational cost. For comparison, a conventional full-aperture reference metalens designed for 1200 nm, with the same diameter and focal length, was also simulated under identical conditions.

As shown in Supplementary Fig. 14(b–d), the reference metalens exhibits diffraction-limited imaging performance only at its design wavelength, while significant chromatic aberrations arise when illuminated at wavelengths several hundred nanometres away. In contrast, the DMM-based metalens maintains proper imaging functionality for each wavelength channel, despite a reduction in intensity associated with the shared aperture (e-f). In all cases, Group 4 elements of the USAF target remain clearly resolvable, confirming that each spectral share independently performs its intended imaging function. Moreover, under simultaneous three-wavelength illumination, the DMM-based metalens continues to form a well-defined image, as all wavelength shares are designed to operate at the same focal distance. These results validate the effectiveness of the proposed function-isolated, multiwavelength imaging strategy.

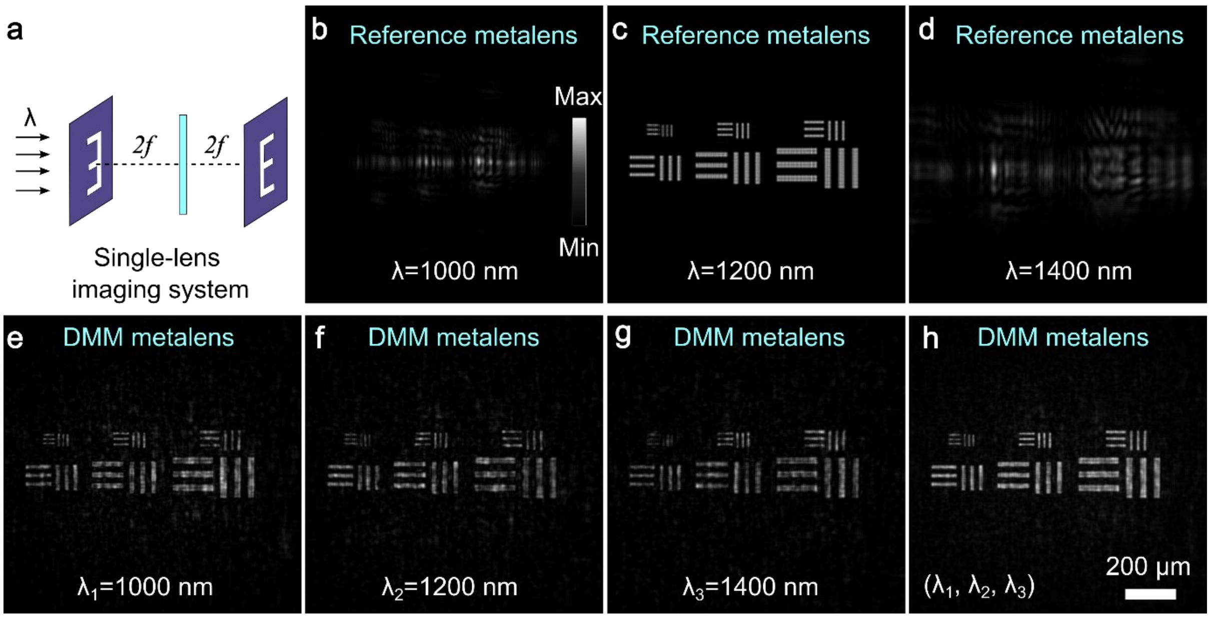

Supplementary Fig. 14. **Single-lens imaging results**. (**a**) Schematic of the single-lens imaging system using coherent laser illumination at wavelength λ. The object and image planes are positioned at twice the focal length (2f). The USAF resolution target (Group 4) imaged using a full-aperture reference metalens designed for 1200 nm and illuminated at (**b**) 1000 nm, (**c**) 1200 nm and (**d**) 1400 nm, respectively. (**e**), (**f**), (**g**) Images of the same resolution target obtained with a three-share DMM-based metalens are shown for comparison. (**h**) Imaging performance of the DMM-based metalens simultaneously at three wavelengths.

G. Wavelength distinct multifunctional display

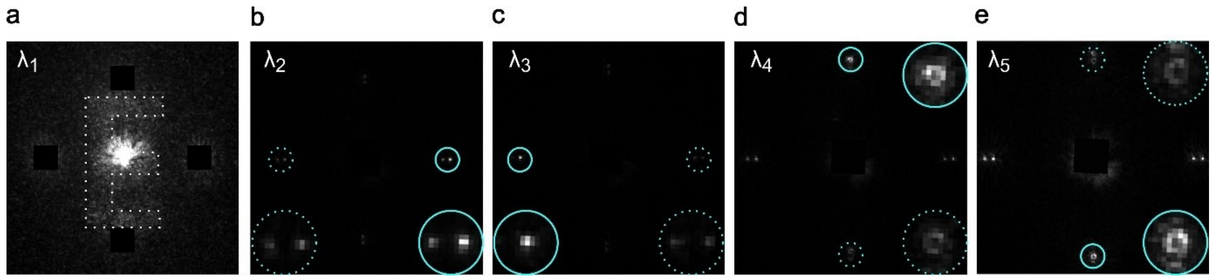

Supplementary Fig. 15. Wavelength distinct multifunction display metasurface. (**a**) display of a holographic image of letter "E" when illuminate with wavelength λ_1. Two independent gratings (**b** and **c**) when illuminate with wavelength λ_2 and λ_3. Two distinct OAM modes (**d** and **e**) when illuminate with wavelength λ_4 and λ_5. The solid circles highlight their target displays.

Supplementary Note 4. IMPLEMENTATION OF DMM-BASED POLARIMETRIC METASURFACE

A. Meta-atom library

We performed a parametric sweep using an in-house RCWA program to determine the required meta-atom dimensions for six grating functions, grouped into three sets corresponding to three shares. An 8×8 meta-atom library was developed for the polarimetric metasurface design (Supplementary Fig. 16). The selected 8×8 meta-atoms cover a 0–2π phase range in both x (Φx) and y (Φy) directions, with an average co-polarisation transmittance exceeding 80%. For each selected meta-atom, the rectangular pillar shape is designed accordingly. For diagonal and anti-diagonal linear polarisations, meta-pillars are rotated by 45° and 135°, respectively. For circular polarisation, meta-atoms with a phase retardance (Φx − Φy) of π are selected.

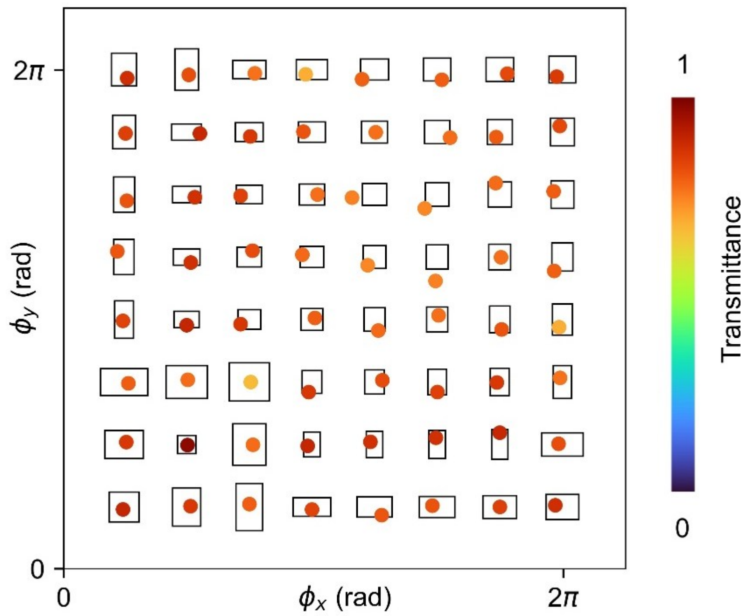

Supplementary Fig. 16. **Meta-atom library for polarimetric samples in Figure 5.** Rectangle shapes at each phase spot represent their corresponding nanopillar geometry.

B. Optical setup for *k*-space imaging

The polarimetric metasurface samples are characterized using a customized k-space imaging setup (Supplementary Fig. 17). To generate the target polarisation, a pair of motorized half-waveplate and quarter-waveplate, mounted on rotation stages (not shown in the schematics), are employed. For structured light generation, a spatial light modulator (SLM) is used. To capture large angles, a low-NA objective lens (10x, NA 0.26) is selected for imaging.

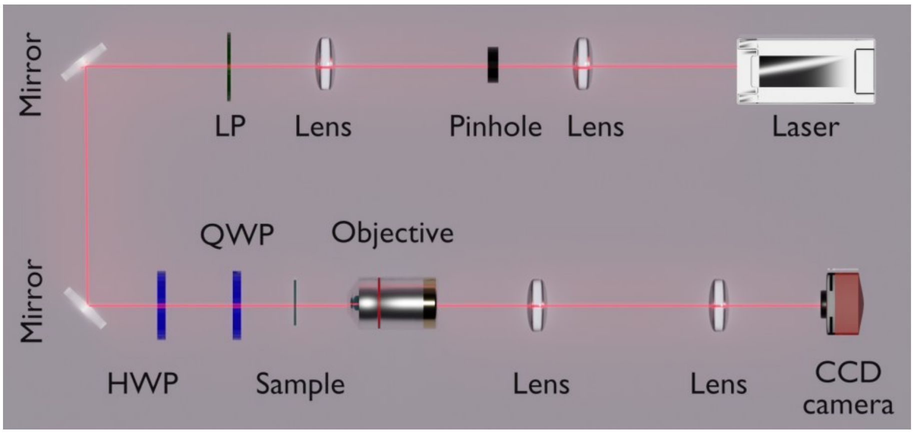

Supplementary Fig. 17. Optical setup for polarimetric metasurface characterisation. Schematic of the k-space polarisation projection configuration.

C. Single-shot polarisation detection with DMM-based metasurface

1. Six fundamental polarisation states

The six fundamental polarisation states, comprising linear and circular polarisations, are characterized: horizontal (H), vertical (V), diagonal (D), and anti-diagonal (A) for linear polarisation, and left-handed (L) and right-handed (R) for circular polarisation. In k-space, the metasurface projects these three orthogonal polarisation bases into six Gaussian-shaped spots (Supplementary Fig. 18. By analysing the relative intensities of these projections, we reconstructed the full Stokes parameters for each incident polarisation state. Using these six base polarisation states as references, we can characterize all arbitrary polarisation states on the Poincaré sphere.

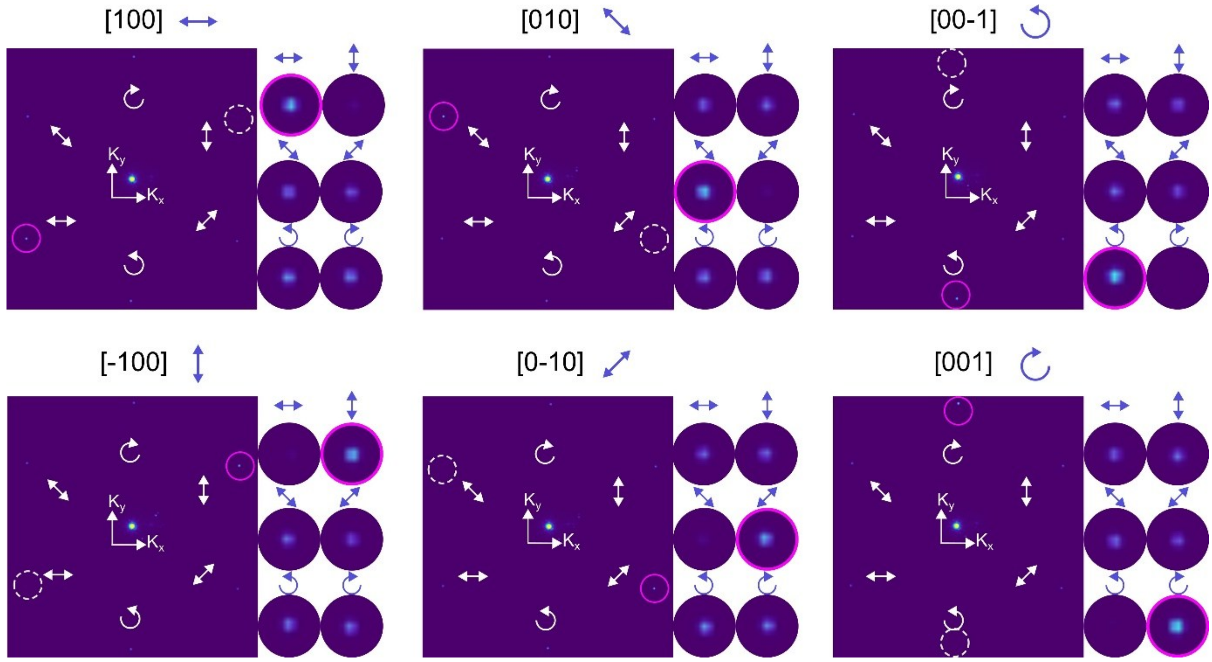

Supplementary Fig. 18. **K-space images of fundamental linear and circular polarisation projections**. Their projection spots zoomed respectively. Red circles indicate the target polarisation (bright) state while dash white circles indicate their orthogonal states (dark). Write arrows indicate the designed polarisation.

2. 100 polarisation states on Poincaré sphere

We systematically generated 100 datasets from the Poincaré sphere, producing corresponding polarisation states by rotating half- and quarter-waveplates (using electric rotating stages synchronized with a camera via a Python program). The measured k-space images were analysed using the aforementioned method to retrieve Stokes parameters. The target and retrieved [S1, S2, S3] coordinates are plotted together. As shown in Supplementary Fig. 19, the experimentally retrieved results closely match the target states on the Poincaré sphere, with a negligible average Stokes parameter mismatch error of 0.039±0.017.

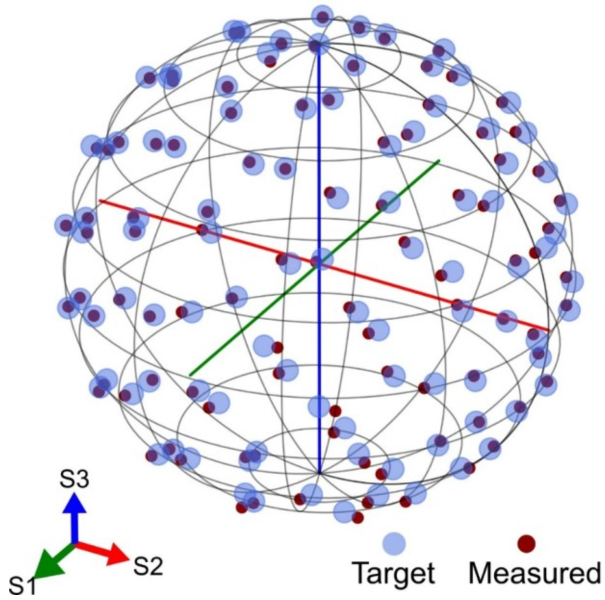

Supplementary Fig. 19. **Detection of 100 polarisation states on a Poincare sphere**. Both target and measured polarisation states, represented by three Stokes parameters, are plotted for compensation.

3. Minimal area for polarimetric imaging

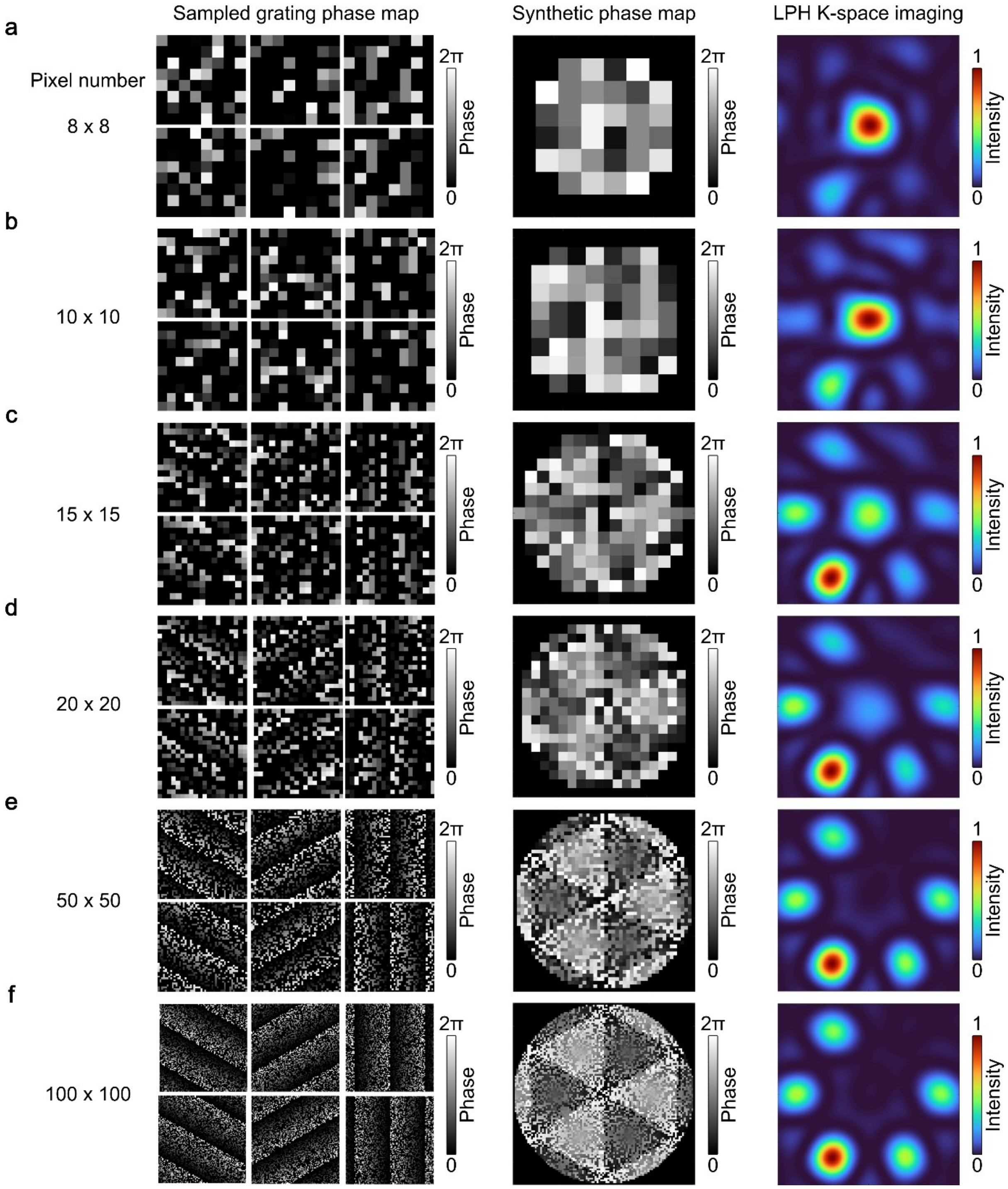

Supplementary Fig. 20. Simulated polarimetric metasurface polarisation projection performance with total pixel number increase from 8x8 (a) to 100x100 (f). Left, sampled grating phase maps. Middle, synthetic grating phase map from three non-orthogonally polarised maps. Right, K-space images of horizontal polarisation projection.

4. Additional complex vector fields imaging

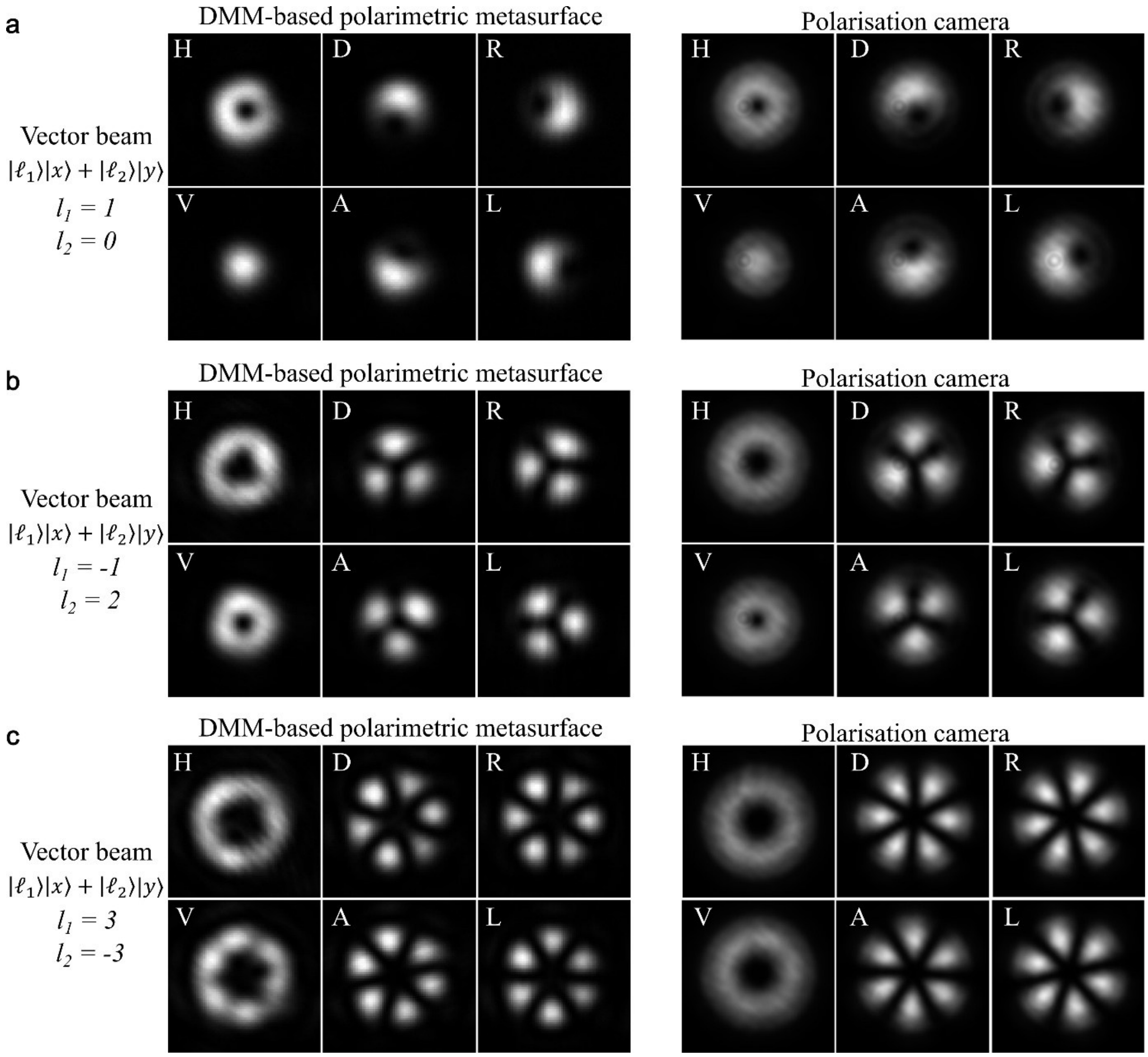

Supplementary Fig. 21. Measured vector field polarisation projection. (**a**), (**b**) and (**c**) are different vector fields synthesised from two original vector fields that carrying different topological chargers (*l*). Left and right panel represents results from our polarimetric and commercial polarimetric camera respectively.

5. Stereographic projections of polarisation skyrmion

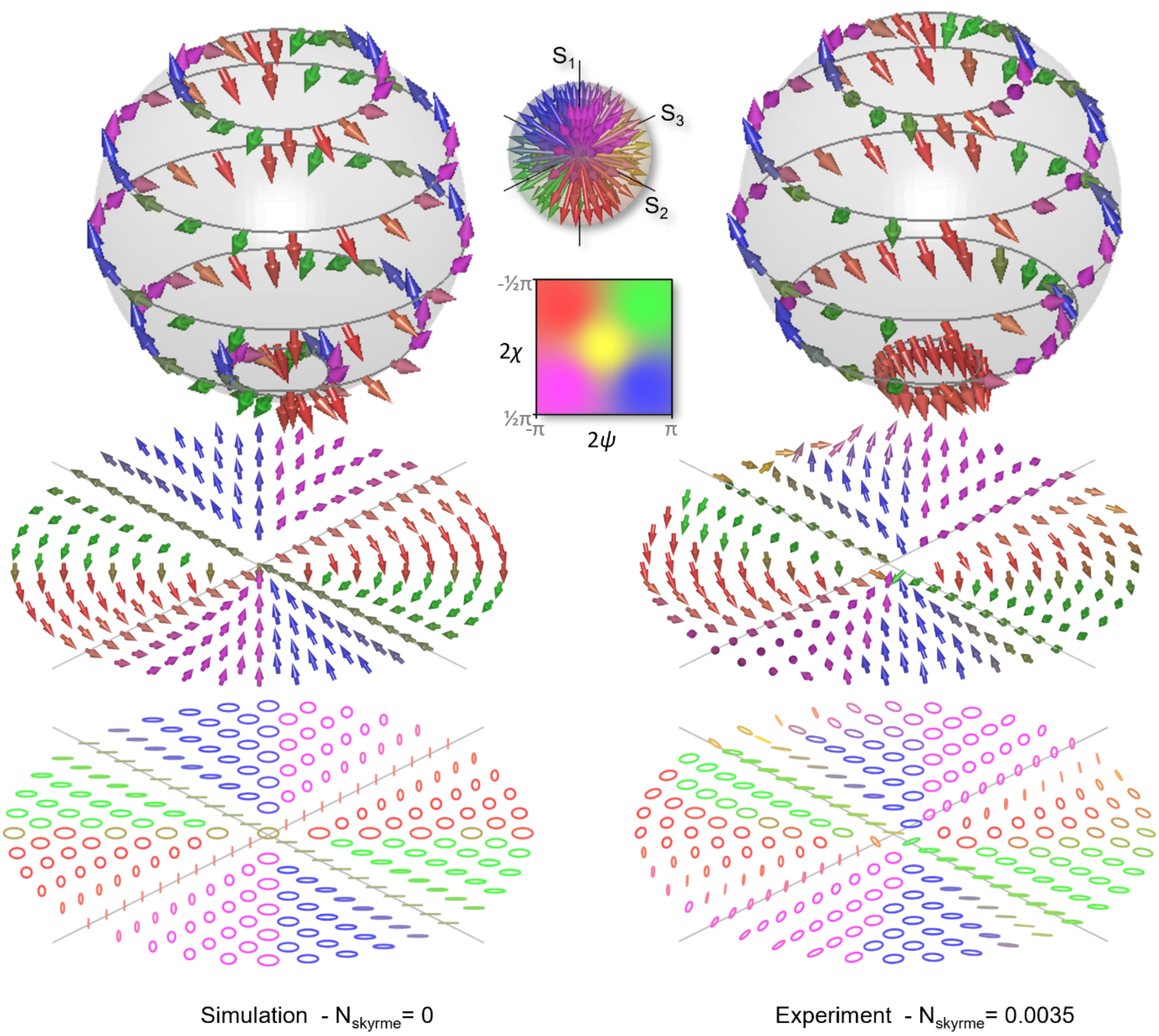

Supplementary Fig. 22. **Additional stereographic projection data set 1.** Theoretical (left) and experimental (right) stereographic projections of a vector beam with a Skyrme/wrapping number of 0.

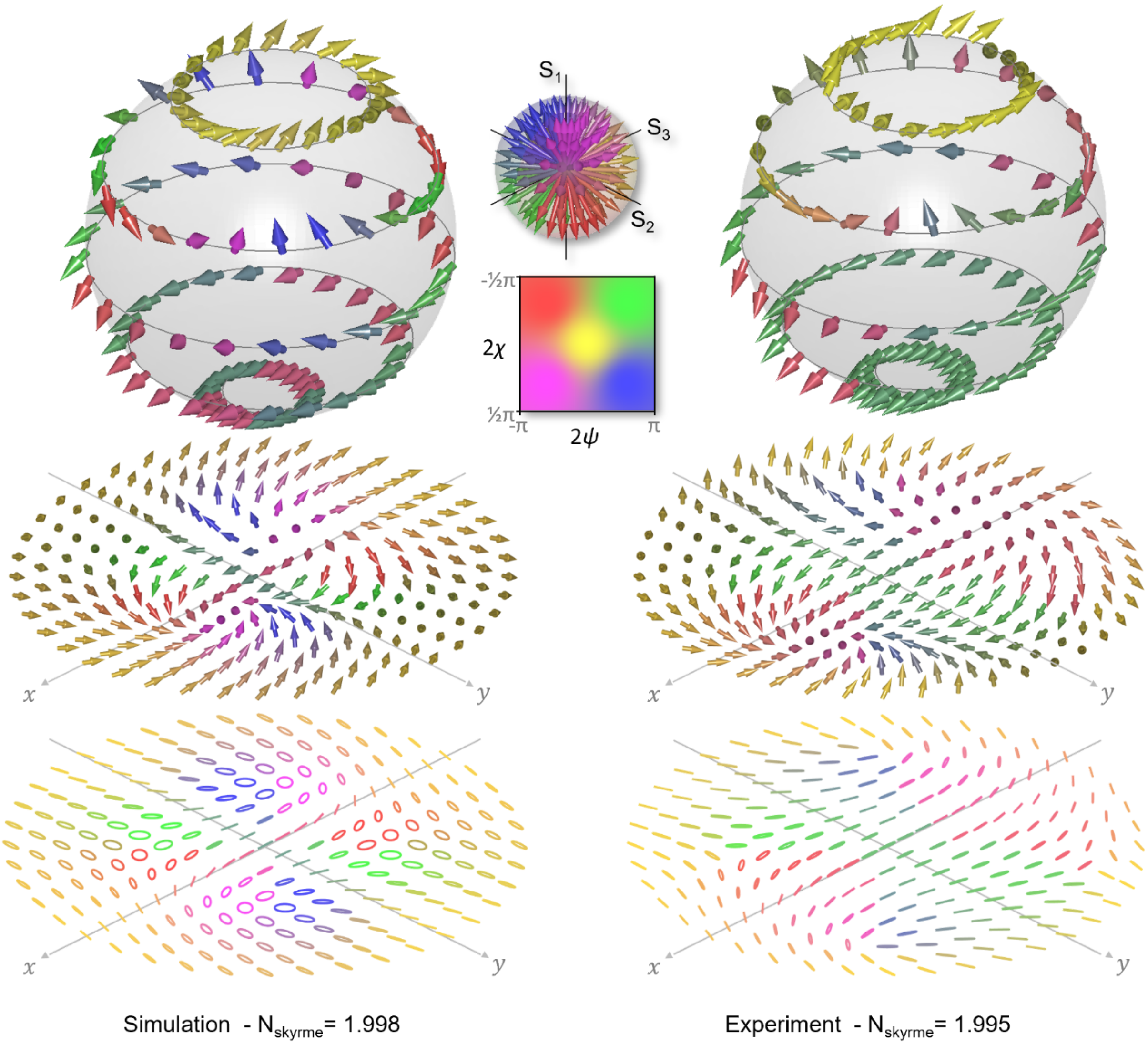

Supplementary Fig. 23. **Additional stereographic projection data set 2.** Theoretical (left) and experimental (right) stereographic projections of a polarisation skyrmion with a Skyrme number of 2.

D. Concurrence modulation and Skyrme number modulation

A key metric for quantifying vector modes is concurrence, which measures the beam's degree of non-separability. Here, we demonstrate modulation of concurrence from C = 0 (fully scalar and separable) to C = 1 (fully vector and non-separable). As shown in Supplementary Fig. 24, the metasurface performs comparably to the polarisation camera for both vector modes and skyrmions.

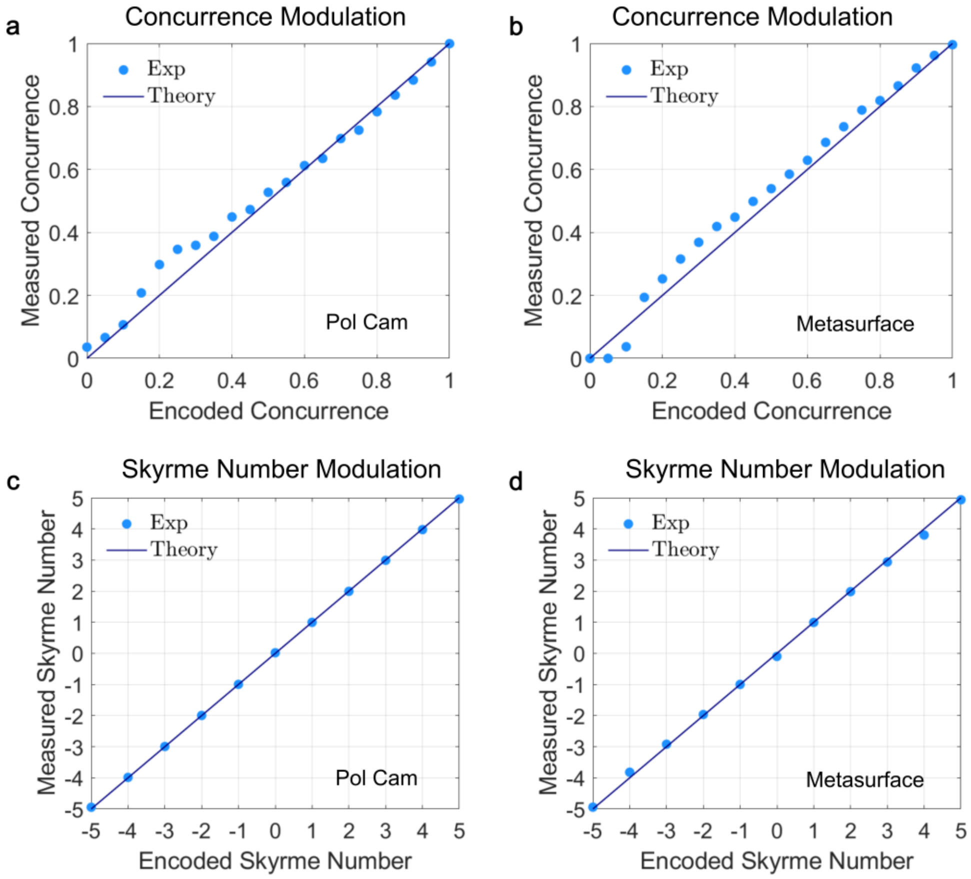

Supplementary Fig. 24. Concurrence modulation and Skyrme number modulation. Experimental and theoretical results for (a, c) polarisation camera and (b, d) our polarimetric metasurface.

The results were taken with a vectorial combination of $l_H = 1$ and $l_V = -1$ where $|\Psi\rangle = \sqrt{a}|\mathrm{l} = 1\rangle|\mathrm{H}\rangle + \sqrt{1-a^2}|\mathrm{l} = -1\rangle|\mathrm{V}\rangle$. to avoid issues of efficiency and the concurrence was encoded power changing the relative powers of the modes in the vectorial superposition according to $C = \sqrt{a(1-a)}$.

Much interest has been put into studying optical Stokes skyrmions. The skyrmions were formed through a vectorial combination of $|\Psi\rangle = |0\rangle|\mathrm{H}\rangle + |l\rangle|\mathrm{V}\rangle$, where l was changed to alter the wrapping number. Here we show results of how the metasurface compares when it comes to measuring the wrapping number of various skyrmionic beams. We see that the metasurface and polarisation camera perform comparably well.

Supplementary Table 1. Wavelengths selected for the synthesis of the multiwavelength metalens in Figure 2f

Wavelength	Region	Significance / Applications
473 nm	Blue (VIS)	Solid-state/DPSS laser line (frequency-doubled 946 nm). Used for fluorescence excitation (e.g. GFP in biology), Raman spectroscopy, high-resolution microscopy, and data storage.
514 nm	Green (VIS)	Argon-ion laser line (514.5 nm). Widely used in Raman spectroscopy, holography, confocal microscopy, and remote sensing of vegetation (matches chlorophyll absorption).
633 nm	Red (VIS)	He–Ne laser line. Benchmark for interferometry, holography, optical alignment, and biomedical optics. Close to the "R" channel in RGB imaging.
1350 nm	NIR (SWIR edge)	Falls in the biological "NIR-II" window → deeper tissue penetration and reduced scattering compared to visible. Useful in OCT, in vivo imaging, and moisture/biomolecule sensing.
1550 nm	NIR (C-band)	Telecom gold standard (lowest fibre loss, eye-safe). Widely used in long-haul fibre optics, LIDAR, free-space optical comms. Standard ITU band.
2050 nm	SWIR	Coincides with CO_2 absorption band → used in atmospheric CO_2 LIDAR, gas sensing, and spectroscopy. Also relevant for eye-safe LIDAR and Tm-fibre medical lasers.
2940 nm	Mid-IR	Er:YAG laser line. Matches strongest water absorption → cornerstone for medical lasers (dermatology, ophthalmology, dentistry, surgery). Also probes O–H vibrations in IR spectroscopy.
3400 nm	Mid-IR	Strong C–H stretch absorption region (~3.3–3.4 µm). Widely used in hydrocarbon detection (methane, other organics) and chemical sensing. Also accessible via He–Ne IR lasers (3.39 µm). Important for environmental monitoring and IR comms experiments.
4000 nm	Mid-IR	Lies in the 4.0 µm atmospheric window, used in thermal remote sensing (e.g. MODIS sea-surface temperature bands). Also near strong CO_2 absorption (~4.26 µm). Relevant in IR astronomy, Earth observation, and military IR sensors.

Supplementary Table 2. Summary of focusing performance of the achromatic metalens in Figure 4

Channel	Wavelength (nm)	PSF FWHM (μm)	Strehl ratio	Sidelobe/Main-lobe ratio
1	1200	6.82 ± 0.06	0.809 ± 0.006	0.064
2	1220	5.98 ± 0.15	0.705 ± 0.015	0.159
3	1240	6.18 ± 0.11	0.793 ± 0.012	0.107
4	1260	5.65 ± 0.14	0.755 ± 0.016	0.162
5	1280	6.32 ± 0.17	0.771 ± 0.017	0.157
6	1300	5.43 ± 0.14	0.859 ± 0.019	0.151
7	1320	5.38 ± 0.14	0.871 ± 0.019	0.132
8	1340	6.55 ± 0.25	0.794 ± 0.025	0.239
9	1360	6.23 ± 0.18	0.789 ± 0.019	0.217
10	1380	6.40 ± 0.17	0.759 ± 0.017	0.181
11	1400	8.82 ± 0.34	0.623 ± 0.019	0.298

Supplementary Table 3. Comparison between existing achromatic metalenses and ours

Ref.	Diameter (mm)	NA	Bandwidth (nm)	Thickness	Dispersion Engineering
Ref. [7]	0.220	0.02	470-670	~ λ	Yes. Large meta-atom library;
Ref. [8]	0.0550	0.106	400-660	~ λ	Yes. Large meta-atom library;
Ref. [9]	0.400	0.02	400-700	~ 10λ	Yes. Large meta-atom library + dispersion-matched layers
Ref. [10]	10	0.7	480-680	~ λ	Yes. Large meta-atom library (training) + inverse design;
Ref. [11]	10.24	0.3	400-1100	> 10λ	Yes. Algorithm optimisation;
Ref. [12]	10	0.7	450-635	~ λ	Yes. Topological inverse design;
Our work	**8.1, no limit**	**0.15**	**1200-1400**	**~0.1λ**	**No need.**

Supplementary Table 4. Comparison between existing polarimetric metasurfaces and ours

Ref.	Minimum meta-atom number	Computational cost	Error of Stokes parameters	Operation bandwidth (centra wavelength)	Single-shot vector beam imaging
Ref. [13]	All sections	Low.	~ 0.01	Narrow (~850 nm)	No
Ref. [14]	One block (11 by 11 meta-atoms).	High. Complex optimisation	< 0.1	10 nm (~532 nm)	No
Ref. [15]	Whole metasurface (complex polarisation reconstruction)	high. Spatial layout arrangement	~ 0.01	400-700 nm	No
Ref. [16]	One block (11 by 11 meta-atoms)	High. Complex optimisation	~ 0.01	30 nm (~940 nm)	No
Our work	**Any continuous 8 by 8 meta-atoms**	**Low.**	**~ 0.04**	**Narrow (~810 nm)**	Yes

Supplementary References

[1] Goodman, Joseph W. Introduction to Fourier optics. Roberts and Company publishers, 2005.

[2] Cliff, Andrew David, and J. Keith Ord. "Spatial processes: models & applications." ((Pion Limited, 1981).

[3] Malek, Stephanie C., et al. "Multifunctional resonant wavefront-shaping meta-optics based on multilayer and multi-perturbation nonlocal metasurfaces." Light: Science & Applications 11.1 (2022): 246.

[4] Wang, Yujie, et al. "High-efficiency broadband achromatic metalens for near-IR biological imaging window." Nature Communications 12.1 (2021): 5560.

[5] Balli, Fatih, et al. "A hybrid achromatic metalens." Nature Communications 11.1 (2020): 3892.

[6] Ren, Haoran, et al. "An achromatic metafiber for focusing and imaging across the entire telecommunication range." Nature Communications 13.1 (2022): 4183.

[7] Chen, Wei Ting, et al. "A broadband achromatic metalens for focusing and imaging in the visible." Nature Nanotechnology 13.3 (2018): 220-226.

[8] Wang, Shuming, et al. "A broadband achromatic metalens in the visible." Nature Nanotechnology 13.3 (2018): 227-232.

[9] Chang, Shengyuan, et al. "Achromatic metalenses for full visible spectrum with extended group delay control via dispersion-matched layers." Nature Communications 15.1 (2024): 9627.

[10] Li, Zhaoyi, et al. "Inverse design enables large-scale high-performance meta-optics reshaping virtual reality." Nature Communications 13.1 (2022): 2409.

[11] Xiao, Xingjian, et al. "Large-scale achromatic flat lens by light frequency-domain coherence optimization." Light: Science & Applications 11.1 (2022): 323.

[12] Choi, Minseok, et al. "Roll-to-plate printable RGB achromatic metalens for wide-field-of-view holographic near-eye displays." Nature Materials (2025): 1-9.

[13] Arbabi, Ehsan, et al. "Full-Stokes imaging polarimetry using dielectric metasurfaces." ACS Photonics 5.8 (2018): 3132-3140.

[14] Rubin, Noah A., et al. "Matrix Fourier optics enables a compact full-Stokes polarisation camera." Science 365.6448 (2019): eaax1839.

[15] Fan, Qingbin, et al. "Disordered metasurface enabled single-shot full-Stokes polarisation imaging leveraging weak dichroism." Nature Communications 14.1 (2023): 7180.

[16] Li, Feng-Jun, et al. "Meta-grating-lens–based monolithic polarization camera." Science Advances 11.43 (2025): eadx9886.